

A Cartesian FMM-accelerated Galerkin boundary integral Poisson-Boltzmann solver

Jiahui Chen¹, Johannes Tausch², Weihua Geng^{2*}

¹*Department of Mathematics, Michigan State University, East Lansing, MI 48824, USA*

²*Department of Mathematics, Southern Methodist University, Dallas, TX 75275, USA*

February 12, 2022

Abstract

The Poisson-Boltzmann model is an effective and popular approach for modeling solvated biomolecules in continuum solvent with dissolved electrolytes. In this paper, we report our recent work in developing a Galerkin boundary integral method for solving the Poisson-Boltzmann (PB) equation. The solver has combined advantages in accuracy, efficiency, and memory usage as it applies a well-posed boundary integral formulation to circumvent many numerical difficulties associated with the PB equation and uses an $O(N)$ Cartesian Fast Multipole Method (FMM) to accelerate the GMRES iteration. In addition, special numerical treatments such as adaptive FMM order, block diagonal preconditioners, Galerkin discretization, and Duffy's transformation are combined to improve the performance of the solver, which is validated on benchmark Kirkwood's sphere and a series of testing proteins.

Keywords: treecode, fast multipole method, electrostatic, boundary integral, Poisson-Boltzmann, preconditioning, GMRES

*Corresponding author. Tel: 1-214-7682252, Fax: 1-214-7682355, Email: wgeng@smu.edu

1 Introduction

In biomolecular simulations, electrostatic interactions are of paramount importance due to their ubiquitous existence and significant contribution in the force fields, which governs the dynamics of molecular simulation. However, computing non-bonded interactions is challenging since these pairwise interactions are long-range with $O(N^2)$ computational cost, which could be prohibitively expensive for large systems. To reduce the degree of freedom of the system in terms of electrostatic interactions, an implicit solvent Poisson-Boltzmann (PB) model is used [1]. In this model, the explicit water molecules are treated as continuum and the dissolved electrolytes are approximated using the statistical Boltzmann distribution. The PB model has broad applications in biomolecular simulations such as protein structure [2], protein-protein interaction [3], chromatin packing [4], pKa [5–7], membrane [8], binding energy [9], solvation free energy [10], ion channel profiling [11], etc.

The PB model is an elliptic interface problem with several numerical difficulties such as discontinuous dielectric coefficients, singular sources, a complex interface, and unbounded domains. Grid-based finite difference or finite volume discretization that discretize the entire volumetric domain have been developed in, e.g., [12–18]. The grid-based discretization is efficient and robust and is therefore popular. However, solvers that are based on discretizing the partial differential equation may suffer from accuracy reduction due to discontinuity of the coefficients, non-smoothness of the solution, singularity of the sources, and truncation of the domains, unless special interface [19, 20] and singularity [21–24] treatments are applied. These treatments come at the price of more complicated discretization scheme and possibly reduced convergence speed of the iterative solver for the linear system.

An alternative approach is to reformulate the PB equation as a boundary integral equation and use the boundary elements to discretize the molecular surface, e.g. [25–33]. Besides the reduction from three dimensional space to the two dimensional molecular boundary, this approach has the advantage that singular charges, interface conditions, and far-field condition are incorporated analytically in the formulation, and hence do not impose additional approximation errors.

In addition, due to the structures hidden in the linear algebraic system after the discretization of the boundary integral and molecular surface, the matrix-vector product in each iteration can be accelerated by fast methods such as fast multipole methods (FMM) [26, 27, 29, 34, 35] and treecodes [36–38]. Our recently developed treecode-accelerated boundary integral (TABI) Poisson-Boltzmann solver [31] is an example of a code that combines the advantages of both boundary integral equation and multipole methods. The TABI solver uses the well-posed derivative form of the Fredholm second kind integral equation [25] and the $O(N \log N)$ treecode [37]. It also has advantages in memory use and parallelization [31, 39]. The TABI solver has been used by many computational biophysics/biochemistry groups and it has been disseminated as a standalone code [31] or as a contributing module of the popular APBS software package [40, 41].

Recently, based on feedback from TABI solver users and our gained experience in theoretical development and practical applications, we realized that we could still improve the TABI solver in the following aspects. First, the $O(N \log N)$ treecode can be replaced by the $O(N)$ FMM method with manageable extra costs in memory usage and complexity of the algorithms. Second, the singularity that occurs when the Poisson’s or Yukawa’s kernel is evaluated was previously handled by simply removing the singular triangle [27, 31] in fact can be treated by using the Duffy transformation [42] analytically, achieving improved accuracy. Third, the collocation scheme used in TABI solver can be updated by using Galerkin discretization with further advantage in maintaining desired accuracy. Fourth, the treecode-based preconditioning scheme that was used in TABI solver [43] can be similarly developed and used under the FMM frame, receiving significant improvement in convergence and robustness. By combining all these new features, we developed a Cartesian fast multipole method (FMM) accelerated Galerkin boundary integral (FAGBI) Poisson-Boltzmann solver. In the remainder

of this article, we provide more detail about the theoretical background of the numerical algorithms related to the FAGBI solver. We conclude with a discussion of the numerical results obtained with our implementation.

2 Theory and Algorithms

In this section we briefly describe the Poisson-Boltzmann (PB) implicit solvent model and review the boundary integral form of the PB equation and its Galerkin discretization. Based on this background information, we then provide details of our recently developed FMM-accelerated Galerkin boundary integral (FAGBI) Poisson-Boltzmann solver, which involves the boundary integral form, multipole expansion scheme, and a block diagonal preconditioning scheme.

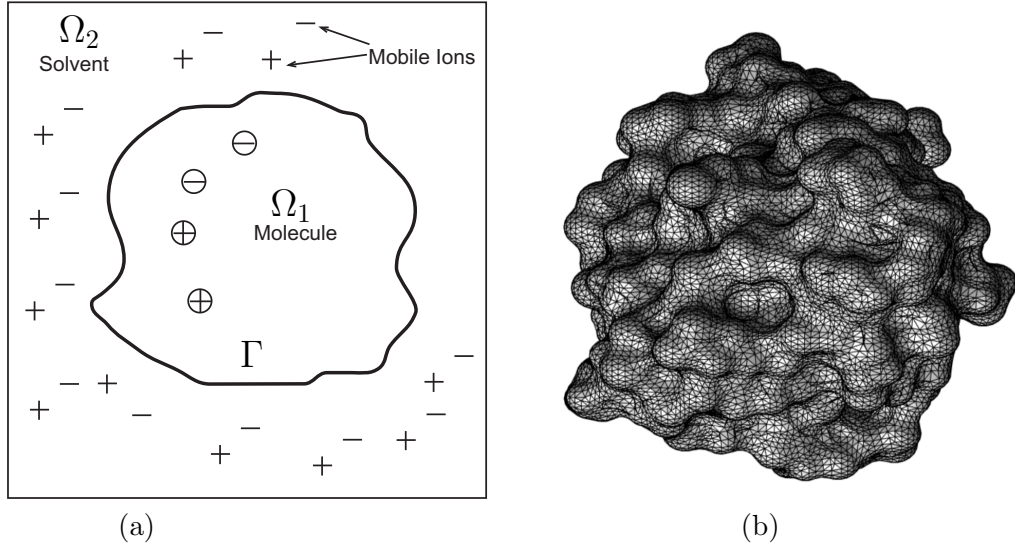


Figure 1: Schematic models; (a) the PB implicit solvent model, in which the molecular surface Γ separates space into the solute region Ω_1 and solvent region Ω_2 ; (b) the triangulation of molecular surface of protein Barstar at MSMS [44] density $d = 5$ (# of vertices per \AA^2).

2.1 The Poisson-Boltzmann (PB) model for a solvated biomolecule

The PB model for a solvated biomolecule is depicted in Fig. 1(a) in which the molecular surface Γ separates the solute domain Ω_1 from the solvent domain Ω_2 . Figure 1(b) is an example of the molecular surface Γ as the triangulated surface of protein barstar [45]. In domain Ω_1 , the solute is represented by N_c partial charges q_k located at atomic centers \mathbf{r}_k for $k = 1, \dots, N_c$, while in domain Ω_2 , a distribution of ions is described by a Boltzmann distribution and we consider a linearized version in this study. The solute domain has a low dielectric constant ϵ_1 and the solvent domain has a high dielectric constant ϵ_2 . The modified inverse Debye length $\bar{\kappa}$ is given as $\bar{\kappa}^2 = \epsilon_2 \kappa^2$, where κ is the inverse Debye length measuring the ionic strength; $\bar{\kappa} = 0$ in Ω_1 and is nonzero only in Ω_2 . The

electrostatic potential $\phi(\mathbf{x})$ satisfies the linear PB equation,

$$-\nabla \cdot \epsilon(\mathbf{x}) \nabla \phi(\mathbf{x}) + \kappa^2(\mathbf{x}) \phi(\mathbf{x}) = \sum_{k=1}^{N_c} q_k \delta(\mathbf{x} - \mathbf{x}_k), \quad (1)$$

subject to continuity conditions for the potential and electric flux density on Γ ,

$$[\phi] = 0, \quad [\epsilon \phi_\nu] = 0, \quad (2)$$

where $[f] = f_1 - f_2$ is the difference of the quantity f across the interface, and $\phi_\nu = \partial \phi / \partial \nu$ is the partial derivative in the outward normal direction ν . The model also incorporates the far-field condition,

$$\lim_{\mathbf{x} \rightarrow \infty} \phi(\mathbf{x}) = 0. \quad (3)$$

Note that Eqs. (1)-(3) define a boundary value problem for the potential $\phi(\mathbf{x})$ which in general must be solved numerically.

2.2 Boundary integral form of PB model

This section summarizes the well-conditioned boundary integral form of the PB implicit solvent model we employ [25, 31]. Applying Green's second identity and properties of fundamental solutions to Eq. (1) yields the electrostatic potential in each domain,

$$\phi(\mathbf{x}) = \int_{\Gamma} \left[G_0(\mathbf{x}, \mathbf{y}) \frac{\partial \phi(\mathbf{y})}{\partial \nu} - \frac{\partial G_0(\mathbf{x}, \mathbf{y})}{\partial \nu_{\mathbf{y}}} \phi(\mathbf{y}) \right] dS_{\mathbf{y}} + \sum_{k=1}^{N_c} q_k G_0(\mathbf{x}, \mathbf{y}_k), \quad \mathbf{x} \in \Omega_1, \quad (4a)$$

$$\phi(\mathbf{x}) = \int_{\Gamma} \left[-G_{\kappa}(\mathbf{x}, \mathbf{y}) \frac{\partial \phi(\mathbf{y})}{\partial \nu} + \frac{\partial G_{\kappa}(\mathbf{x}, \mathbf{y})}{\partial \nu_{\mathbf{y}}} \phi(\mathbf{y}) \right] dS_{\mathbf{y}}, \quad \mathbf{x} \in \Omega_2, \quad (4b)$$

where $G_0(\mathbf{x}, \mathbf{y})$ and $G_{\kappa}(\mathbf{x}, \mathbf{y})$ are the Coulomb and screened Coulomb potentials,

$$G_0(\mathbf{x}, \mathbf{y}) = \frac{1}{4\pi|\mathbf{x} - \mathbf{y}|}, \quad G_{\kappa}(\mathbf{x}, \mathbf{y}) = \frac{e^{-\kappa|\mathbf{x} - \mathbf{y}|}}{4\pi|\mathbf{x} - \mathbf{y}|}, \quad (5)$$

and $\mathbf{y}_k \in \Omega_1$ are the location of the atomic centers.

Applying the interface conditions in Eq. (2) with the differentiation of electrostatic potential in each domain yield a set of boundary integral equations relating the surface potential ϕ_1 (the subscript 1 denotes the inside domain) and its normal derivative $\partial \phi_1 / \partial \nu$ on Γ , [25, 31],

$$\frac{1}{2} (1 + \varepsilon) \phi_1(\mathbf{x}) = \int_{\Gamma} \left[K_1(\mathbf{x}, \mathbf{y}) \frac{\partial \phi_1(\mathbf{y})}{\partial \nu} + K_2(\mathbf{x}, \mathbf{y}) \phi_1(\mathbf{y}) \right] dS_{\mathbf{y}} + S_1(\mathbf{x}), \quad \mathbf{x} \in \Gamma, \quad (6a)$$

$$\frac{1}{2} \left(1 + \frac{1}{\varepsilon} \right) \frac{\partial \phi_1(\mathbf{x})}{\partial \nu} = \int_{\Gamma} \left[K_3(\mathbf{x}, \mathbf{y}) \frac{\partial \phi_1(\mathbf{y})}{\partial \nu} + K_4(\mathbf{x}, \mathbf{y}) \phi_1(\mathbf{y}) \right] dS_{\mathbf{y}} + S_2(\mathbf{x}), \quad \mathbf{x} \in \Gamma, \quad (6b)$$

where $\varepsilon = \varepsilon_2 / \varepsilon_1$, and the kernels $K_{1,2,3,4}$ and source terms $S_{1,2}$ are

$$K_1(\mathbf{x}, \mathbf{y}) = G_0(\mathbf{x}, \mathbf{y}) - G_{\kappa}(\mathbf{x}, \mathbf{y}), \quad K_2(\mathbf{x}, \mathbf{y}) = \varepsilon \frac{\partial G_{\kappa}(\mathbf{x}, \mathbf{y})}{\partial \nu_{\mathbf{y}}} - \frac{\partial G_0(\mathbf{x}, \mathbf{y})}{\partial \nu_{\mathbf{y}}}, \quad (7a)$$

$$K_3(\mathbf{x}, \mathbf{y}) = \frac{\partial G_0(\mathbf{x}, \mathbf{y})}{\partial \nu_{\mathbf{x}}} - \frac{1}{\varepsilon} \frac{\partial G_{\kappa}(\mathbf{x}, \mathbf{y})}{\partial \nu_{\mathbf{x}}}, \quad K_4(\mathbf{x}, \mathbf{y}) = \frac{\partial^2 G_{\kappa}(\mathbf{x}, \mathbf{y})}{\partial \nu_{\mathbf{x}} \partial \nu_{\mathbf{y}}} - \frac{\partial^2 G_0(\mathbf{x}, \mathbf{y})}{\partial \nu_{\mathbf{x}} \partial \nu_{\mathbf{y}}}, \quad (7b)$$

and

$$S_1(\mathbf{x}) = \frac{1}{\varepsilon_1} \sum_{k=1}^{N_c} q_k G_0(\mathbf{x}, \mathbf{y}_k), \quad S_2(\mathbf{x}) = \frac{1}{\varepsilon_1} \sum_{k=1}^{N_c} q_k \frac{\partial G_0(\mathbf{x}, \mathbf{y}_k)}{\partial \nu_{\mathbf{x}}}. \quad (8)$$

As given in Eqs. (7a-7b) and (8), the kernels $K_{1,2,3,4}$ and source terms $S_{1,2}$ are linear combinations of G_0 , G_k , and their first and second order normal derivatives [25,31]. Since the Coulomb potential is singular, the kernels have the following behavior

$$K_1(\mathbf{x}, \mathbf{y}) = O(1), \quad K_{2,3,4}(\mathbf{x}, \mathbf{y}) = O\left(\frac{1}{|\mathbf{x} - \mathbf{y}|}\right),$$

as $\mathbf{y} \rightarrow \mathbf{x}$.

After the potentials ϕ_1 and $\partial\phi_1/\partial\nu$ have been found by solving the boundary integral equation, the electrostatic solvation energy can be obtained by

$$E_{\text{sol}} = \frac{1}{2} \sum_{k=1}^{N_c} q_k \phi_{\text{reac}}(\mathbf{y}_k) = \frac{1}{2} \sum_{k=1}^{N_c} q_k \int_{\Gamma} \left[K_1(\mathbf{y}_k, \mathbf{y}) \frac{\partial\phi_1(\mathbf{y})}{\partial\nu} + K_2(\mathbf{y}_k, \mathbf{y}) \phi_1(\mathbf{y}) \right] dS_{\mathbf{y}}, \quad (9)$$

where $\phi_{\text{reac}}(\mathbf{x}) = \phi_1(\mathbf{x}) - S_1(\mathbf{x})$ is the reaction potential [25,31].

2.3 Galerkin Discretization

In solving the boundary integral PB equation, both the molecular surface and the solution function need to be discretized. The molecular surface Γ is usually approximated by a collection of triangles

$$\Gamma_N = \bigcup_{i=1}^N \tau_i, \quad (10)$$

where N is number of elements and τ_i for $i = 1, \dots, N$ is a planar triangular boundary element with mid-point \mathbf{x}_i^c . This triangulation must be conforming, i.e., the intersection of two different triangles is either empty, or a common vertex or edge. Fortunately, surface generators are available, and our choice for our computations is MSMS [44], though other packages could also be used. Here, the resolution of the surface can be controlled by the parameter d that controls the number of vertices per \AA^2 . For example, Fig. 1 (b) shows the triangulated molecule surface of the protein barstar, which will bind another protein barnase to form a biomolecular complex (PDB: 1b2s) [45].

Each triangle τ_i of Γ_N is the parametric image of the reference triangle τ

$$\tau = \{ \eta = (\eta_1, \eta_2) \in \mathbb{R}^2 : 0 \leq \eta_1 \leq 1, 0 \leq \eta_2 \leq \eta_1 \}. \quad (11)$$

If \mathbf{u}_i , \mathbf{v}_i and \mathbf{w}_i are the vertices then the parameterization is given by

$$\mathbf{x}(\eta) = \mathbf{u}_i + \eta_1(\mathbf{v}_i - \mathbf{u}_i) + \eta_2(\mathbf{w}_i - \mathbf{u}_i) \in \tau_i \quad \text{for } \eta = (\eta_1, \eta_2) \in \tau. \quad (12)$$

The area of the element, the local mesh size, and the global mesh size of the boundary elements τ_i are given as $A_i = \frac{1}{2} |(\mathbf{v}_i - \mathbf{u}_i) \times (\mathbf{w}_i - \mathbf{u}_i)|$, $h_i = \sqrt{A_i}$, and $h = \max_{1 \leq i \leq N} h_i$.

Since a function f defined on τ_i can be interpreted as a function $g(\eta)$ with respect to the reference element τ ,

$$f(\mathbf{x}) = f(\mathbf{x}(\eta)) = g(\eta) \quad \text{for } \eta \in \tau, \quad \mathbf{x} \in \tau_i. \quad (13)$$

we can define a finite element space by functions on Γ_N whose pullbacks to the reference triangle are polynomials in η . The simplest example is the space of piecewise constant functions, which are

polynomials of order zero on each triangle, which will be denoted by $S_h^0(\Gamma_N)$. Obviously, the dimension of this space is N and the basis is given by the box functions

$$\psi_i^0(\mathbf{x}) = \begin{cases} 1 & \text{if } \mathbf{x} \in \tau_i, \\ 0 & \text{otherwise,} \end{cases} \quad (14)$$

where i is an index of a triangle.

The next step up are piecewise linear functions. Since there are three independent linear functions on τ , namely,

$$\psi_1^1(\eta) = 1 - \eta_1, \quad \psi_2^1(\eta) = \eta_1 - \eta_2, \quad \psi_3^1(\eta) = \eta_2 \quad \text{for } \eta = (\eta_1, \eta_2) \in \tau. \quad (15)$$

the dimension is $3N$. Usually, one works with the space of continuous linear functions, denoted by $S_h^1(\Gamma_N)$. It is not hard to see that the dimension of this space is the number of vertices and that the basis is given by

$$\psi_i^c(\mathbf{x}) = \begin{cases} 1 & \text{for } \mathbf{x} = \mathbf{v}_i, \\ 0 & \text{for } \mathbf{x} = \mathbf{v}_j \neq \mathbf{v}_i, \\ \text{piecewise linear} & \text{elsewhere,} \end{cases} \quad (16)$$

where v_i is the i -th vertex.

The approximation powers of piecewise polynomial spaces are well known, see, e.g., [46]. For a function $w \in H_{pw}^1(\Gamma_N)$ we denote by w_h^0 the L_2 -orthogonal projection of w into the space of piecewise constant functions, then

$$\|w - w_h^0\|_{L_2(\Gamma_N)} \leq c \left(\sum_{i=1}^N h_i^2 |w|_{H^1(\tau_i)}^2 \right)^{\frac{1}{2}} \leq ch |w|_{H_{pw}^1(\Gamma_N)}, \quad (17)$$

where c is the upper bound of the mesh ratio h_{\max}/h_{\min} , h is the maximal diameter of a triangle and

$$|w|_{H_{pw}^1(\Gamma_N)} = \left(\sum_{i=1}^N |w|_{H^1(\tau_i)}^2 \right)^{1/2}. \quad (18)$$

Thus, the constant piecewise basis function can give a convergence rate of maximum $O(h)$.

Likewise, the error for the L_2 -orthogonal projection w_h^1 of $w \in H_{pw}^2(\Gamma_N)$ into $S_h^1(\Gamma_N)$ is

$$\|w - w_h^1\|_{L_2(\Gamma_N)} \leq c \left(\sum_{i=1}^N h_i^2 |w|_{H^2(\tau_i)}^2 \right)^{\frac{1}{2}} \leq ch^2 |w|_{H_{pw}^2(\Gamma_N)}, \quad (19)$$

Finite element spaces with higher order polynomials could also be considered, however their practical value for surfaces with low regularity and complicated geometries is limited.

The Galerkin discretization is based on a variational formulation of integral equations (6a) and (6b). That is, instead of understanding the equations pointwise for $\mathbf{x} \in \Gamma_N$ the equations are multiplied by test functions ψ and ψ^ν and integrated again over Γ_N . Solving the variational form amounts to finding ϕ_1 and $\partial\phi_1/\partial\nu$ such that

$$\int_{\Gamma_N} \left\{ \frac{1}{2} (1 + \varepsilon) \phi_1(\mathbf{x}) - \int_{\Gamma_N} \left[K_1(\mathbf{x}, \mathbf{y}) \frac{\partial\phi_1(\mathbf{y})}{\partial\nu} + K_2(\mathbf{x}, \mathbf{y}) \phi_1(\mathbf{y}) \right] dS_{\mathbf{y}} \right\} \psi(\mathbf{x}) dS_{\mathbf{x}} = \int_{\Gamma_N} S_1(\mathbf{x}) \psi(\mathbf{x}) dS_{\mathbf{x}}, \quad (20a)$$

$$\int_{\Gamma_N} \left\{ \frac{1}{2} \left(1 + \frac{1}{\varepsilon} \right) \frac{\partial\phi_1(\mathbf{x})}{\partial\nu} - \int_{\Gamma_N} \left[K_3(\mathbf{x}, \mathbf{y}) \frac{\partial\phi_1(\mathbf{y})}{\partial\nu} + K_4(\mathbf{x}, \mathbf{y}) \phi_1(\mathbf{y}) \right] dS_{\mathbf{y}} \right\} \psi^\nu(\mathbf{x}) dS_{\mathbf{x}} = \int_{\Gamma_N} S_2(\mathbf{x}) \psi^\nu(\mathbf{x}) dS_{\mathbf{x}}, \quad (20b)$$

holds for all test functions ψ, ψ^ν . In the Galerkin method the solution and the test functions are formally replaced by functions in the finite element space. To that end, the unknowns are expanded by basis functions ψ_i (which could be either box or hat functions)

$$\phi \approx \sum_{i=1}^N \phi_i \psi_i, \quad \text{and} \quad \frac{\partial \phi}{\partial \nu} \approx \sum_{i=1}^N \phi_i^\nu \psi_i \quad (21)$$

and integral equations are tested against the basis functions. This leads to the linear system $Ax = b$ where x contains the coefficients in (21) and

$$A = \begin{bmatrix} A_{11} & A_{12} \\ A_{21} & A_{22} \end{bmatrix} \quad \text{and} \quad b = \begin{bmatrix} b_1 \\ b_2 \end{bmatrix}. \quad (22)$$

The entries of these block matrices are given as

$$\begin{aligned} A_{11}(i, j) &= \int_{\Gamma_N} \frac{1}{2} (1 + \varepsilon) \psi_i(\mathbf{x}) \psi_j(\mathbf{x}) dS_{\mathbf{x}} + \int_{\Gamma_N} \int_{\Gamma_N} K_2(\mathbf{x}, \mathbf{y}) \psi_i(\mathbf{x}) \psi_j(\mathbf{y}) dS_{\mathbf{y}} dS_{\mathbf{x}} \\ A_{12}(i, j) &= \int_{\Gamma_N} \int_{\Gamma_N} K_1(\mathbf{x}, \mathbf{y}) \psi_i(\mathbf{x}) \psi_j(\mathbf{y}) dS_{\mathbf{y}} dS_{\mathbf{x}} \\ A_{21}(i, j) &= \int_{\Gamma_N} \int_{\Gamma_N} K_4(\mathbf{x}, \mathbf{y}) \psi_i(\mathbf{x}) \psi_j(\mathbf{y}) dS_{\mathbf{y}} dS_{\mathbf{x}} \\ A_{22}(i, j) &= \int_{\Gamma_N} \frac{1}{2} \left(1 + \frac{1}{\varepsilon} \right) \psi_i(\mathbf{x}) \psi_j(\mathbf{x}) dS_{\mathbf{x}} + \int_{\Gamma_N} \int_{\Gamma_N} K_3(\mathbf{x}, \mathbf{y}) \psi_i(\mathbf{x}) \psi_j(\mathbf{y}) dS_{\mathbf{y}} dS_{\mathbf{x}} \end{aligned} \quad (23)$$

and the right hand side is

$$b_1(i) = \int_{\Gamma_N} S_1(\mathbf{x}) \psi_i(\mathbf{x}) dS_{\mathbf{x}} \quad \text{and} \quad b_2(i) = \int_{\Gamma_N} S_2(\mathbf{x}) \psi_i(\mathbf{x}) dS_{\mathbf{x}} \quad (24)$$

Since the basis functions vanish on most triangles, the integrations for the coefficients are only local. For instance, for piecewise constant elements, the integral $\int_{\Gamma} \dots \psi_i dS_{\mathbf{x}}$ reduces to $\int_{\tau_i} \dots dS_{\mathbf{x}}$. Since the coefficients cannot be expressed in analytical form they have to be calculated by a suitable choice of quadrature rule. However singularities will appear if triangles τ_i and τ_j are identical or sharing common edges and vertices. To overcome this issue, we apply the singularity removing transformation of [47]. This results smooth integrals over a four dimensional cube. The latter integrals are then approximated by tensor product Gauss-Legendre quadrature.

After the solution of the linear system has been obtained, the electrostatic free solvation energy can be calculated using the approximations for the surface potentials and its normal derivative

$$E_{sol} = \frac{1}{2} \sum_{n=1}^{N_c} q_n \sum_{i=1}^N \int_{\tau_i} \left[K_1(\mathbf{x}_n, \mathbf{x}) \phi_{1i}^\nu + K_2(\mathbf{x}_n, \mathbf{x}) \phi_{1i} \right] dS_{\mathbf{x}}. \quad (25)$$

Since the matrix A is a dense and non-symmetric our choice of solver is the GMRES method. In each step of GMRES iteration, a matrix-vector product is calculated and a direct summation for this requires $O(N^2)$ complexity. Below we will introduce the $O(N)$ Cartesian Fast Multipole Method (FMM) to accelerate the matrix-vector product. Calculating the electrostatic solvation free energy E_{sol} in Eq. (25) is $O(N_c N)$ and we use a Cartesian treecode to reduce the cost to $O(N_c \log(N))$. Both FMM and treecode algorithm are described the next for comparison and for the reason that both are used to accelerate the N-body particle-particle interactions.

2.4 Cartesian fast multipole method (FMM)

In this section, we introduce the Cartesian FMM to evaluate matrix vector products with the matrix in (22) efficiently. This is a kernel-independent version of the FMM, where instead of the multipole expansion, truncated Taylor series are used to approximate Coulomb ($\kappa = 0$) the screened Coulomb ($\kappa \neq 0$) potential.

This considerably simplifies the translation operators for the kernels K_{1-4} because they involve different values of κ . It was shown in [48] how the derivatives of the Coulomb kernel can be computed by simple recurrence formulas. Furthermore, the moment-to-moment (MtM) and local-to-local (LtL) translation are easily derived using the binomial formula.

When a refined mesh is required for a larger N , increasing the expansion order is essential to control the accuracy. The FMM error analysis implies that the truncated Taylor expansion error has the same magnitude as the discretization error if the expansion order is adjusted to the level according to the formula

$$p_l = p_L + L - l \quad (26)$$

where $l = 0, 1, \dots, L$ with $l = 0$ the coarsest level and $l = L$ the finest level. That is, the finest level uses a low-order expansion p_L , and the order is incremented in each coarser level, see [35].

Note that the multipole series is more efficient as it contains $(p+1)^2$ terms, while the Taylor series has $p(p+1)(p+2)/6$ terms. This difference becomes significant with larger values of p . However, with the variable order scheme the advantage of the multipole series is much less because most translation operators are in the fine levels where the number of terms in both series are comparable.

The matrix vector product can be considered as generalized N -body problem of the form

$$V_i = \int_{\Gamma_N} \int_{\Gamma_N} \psi_i(\mathbf{x}) \frac{\partial^l}{\partial \nu_{\mathbf{x}}^l} \frac{\partial^k}{\partial \nu_{\mathbf{y}}^k} G(\mathbf{x}, \mathbf{y}) f_h(\mathbf{y}) dS_{\mathbf{y}} dS_{\mathbf{x}}. \quad (27)$$

where $k, l \in \{0, 1\}$ and f_h is a linear combination of the basis functions ψ_j .

Next we show how the Cartesian FMM is used under the framework of boundary element method.

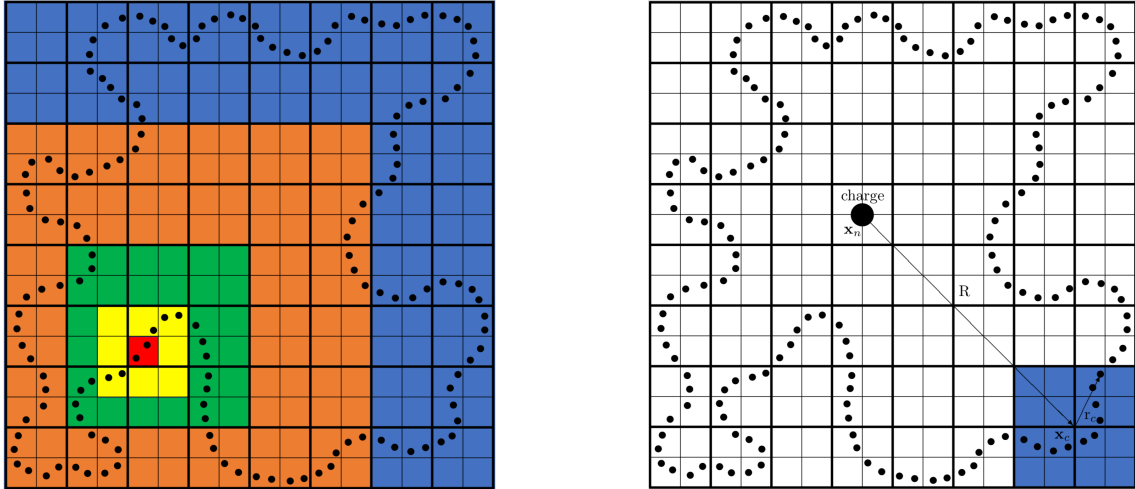


Figure 2: FMM vs Treecode structure. Left: FMM cluster-cluster interaction list; Right: treecode particle-cluster interaction (R is the distance from the charge to the blue cluster's center; r_c is the radius of the blue cluster c which is the farthest particle inside c to the center of c).

Figure 2a is a 2-D illustration of a discretized molecular surface Γ_N embedded in a hierarchy of cubes (squares in the image). Each black solid dot represents a boundary triangle τ_i for $i = 1, \dots, N$.

A cluster c in any level l is defined as the union of triangles whose centroid are located in a cube of that level. C_l is the set of all clusters in level l .

The level-0 cube is the smallest axiparallel cube that contains Γ_N and thus $C_0 = \Gamma_N$. The refinement of coarser cubes into finer cubes stops when clusters in the finest level contain at most a predetermined (small) number of triangles. For a cluster c we denote by B_c the smallest axiparallel rectangular box that contains c and write \mathbf{x}_c for its center and ρ_c for the half-length of its longest diagonal. Note that B_c can be considerably smaller than its cube, this is why we call this process the shrink scheme. For two clusters c and c' in the same level we denote by

$$\eta(c, c') = \frac{\rho_c + \rho_{c'}}{|\mathbf{x}_c - \mathbf{x}_{c'}|} \quad (28)$$

the separation ratio of the two clusters. This number determines the convergence rate of the Taylor series expansion, see [35]. Two clusters in the same level are neighbors if their separation ratio is larger than a predetermined constant. $\mathcal{N}(c)$ denotes the set of its neighbors for a given cluster c . The set of nonempty children of c that are generated in the refinement process is denoted by $\mathcal{K}(c)$. Finally, we use $\mathcal{I}(c)$ to denote the interaction list for a cluster c , which are clusters at the same level such that for any $c' \in \mathcal{I}(c)$, the parent of c' is a neighbor of the parent of c , but c' itself is not a neighbor of c .

Under the FMM framework, the evaluation of Eq. (27) consists of the near field direct summation and the Taylor expansion approximation for well-separated far field. The near field direct summation happens in between neighboring panels in the finest level. The far field summation is done by multipole or Taylor expansions between interaction lists in all levels. This process is described in many papers, so we do not give details about the derivation.

To emphasize the differences of the cartesian FMM, we consider a cluster-cluster interaction between two clusters c and $c' \in \mathcal{I}(c)$. Let u be the potential due to sources in c' which is evaluated in c , then by Taylor expansion of the kernel with center $\mathbf{x} = \mathbf{x}_c$ and $\mathbf{y} = \mathbf{x}_{c'}$ one finds easily that

$$u_{c,c'}(\mathbf{x}) = \int_{c'} \frac{\partial^l}{\partial \nu_{\mathbf{x}}^l} \frac{\partial^k}{\partial \nu_{\mathbf{y}}^k} G(\mathbf{x}, \mathbf{y}) f_h(\mathbf{y}) dS_{\mathbf{y}} \approx \sum_{|\alpha| \leq p} \lambda_c^\alpha \frac{\partial^l}{\partial \nu_{\mathbf{x}}^l} (\mathbf{x} - \mathbf{x}_c)^\alpha. \quad (29)$$

where and $\alpha = (\alpha_1, \alpha_2, \alpha_3) \in \mathbb{N}^3$ is a multi-index. The expansion coefficients are given by

$$\lambda_c^\alpha = \sum_{|\beta|=0}^{p-|\alpha|} \frac{D^{\alpha+\beta} G(\mathbf{x}_c, \mathbf{x}_{c'})}{\alpha! \beta!} (-1)^\beta m_{c'}^\beta(f_h), \quad |\alpha| \leq p. \quad (30)$$

where $\alpha! = \alpha_1! \alpha_2! \alpha_3!$ and $m_{c'}^\beta(f)$ is the moment of f_h , given by

$$m_{c'}^\beta(f) = \int_{S_{c'}} \frac{\partial^k}{\partial \nu_{\mathbf{x}}^k} (\mathbf{x} - \mathbf{x}_{c'})^\beta f_h(\mathbf{x}) dS_{\mathbf{x}}, \quad |\beta| \leq p. \quad (31)$$

Equation (30) translates the moment of c' to the local expansion coefficients of the cluster c , and it is therefore called MtL translation. Since f_h is a linear combination of basis functions, we obtain from linearity that

$$m_{c'}^\beta(f) = \sum_{i \in c'} m_{c'}^\beta(\psi_i) f_i \quad (32)$$

where f_i are the coefficients of f_h with respect to the ψ_i -basis and the summation is taken over basis functions that whose support overlaps with c . Since we consider a Galerkin discretization we have

to integrate the function $u_{c,c'}(\mathbf{x})$ against the test functions, to obtain the contribution g_i of the two clusters to the matrix vector product. Thus we get from (29)

$$g_i = \int_c \psi_i(\mathbf{x}) u_{c,c'}(\mathbf{x}) dS_{\mathbf{x}} = \sum_{|\alpha| \leq p} \lambda_c^\alpha \int_c \frac{\partial^l}{\partial \nu_{\mathbf{x}}^l} (\mathbf{x} - \mathbf{x}_c)^\alpha \psi_i(\mathbf{x}) dS_{\mathbf{x}} = \sum_{|\alpha| \leq p} \lambda_c^\alpha m_c^\alpha(\psi_i) \quad (33)$$

This operation converts expansion coefficients to potentials and is denoted as LtP translation.

To move moments and local expansion coefficients between levels, we also need the moment-to-moment (MtM) and local-to-local (LtL) translations. They can be derived easily from the multivariate binomial formula. We obtain

$$m_c^\alpha(f) = \sum_{c' \in \mathcal{K}(c)} \sum_{\beta \leq \alpha} \binom{\alpha}{\beta} (\mathbf{x}_{c'} - \mathbf{x}_c)^{\alpha-\beta} m_{c'}^\beta(f), \quad (34)$$

and

$$\lambda_{c'}^\beta = \sum_{\substack{\alpha \leq \beta \\ |\alpha| \leq p}} \binom{\alpha}{\beta} (\mathbf{x}_{c'} - \mathbf{x}_c)^{\alpha-\beta} \lambda_c^\alpha, \quad |\beta| \leq p. \quad (35)$$

where $c' \in \mathcal{K}(c)$.

We see that moments and expansion coefficients are computed by recurrence from the previous level. In the finest level the moments of the basisfunctions $m_c(\psi_i)$ can be either computed by numerical quadrature, or even analytically, because we consider flat panels and polynomial ansatz functions. We skip the details, as these formulas are straightforward application of the binomial formula.

In summary, the Cartesian FMM under the framework of boundary element method is described as the following.

1. *Nearfield Calculation.*
for $c \in C_L$
for $c' \in \mathcal{N}(c)$
multiply matrix block of c and c' directly.
2. *Moment Calculation.*
for $c \in C_L$
Compute the moments $m_{c'}^\beta(f)$ in (32).
3. *Upward Pass.*
for $l = L - 1, \dots, l_{min}$
for $c \in C_l$
for $c' \in \mathcal{K}(c)$
Compute the MtM translation (34)
4. *Interaction Phase.*
for $l = L, \dots, l_{min}$
for $\nu \in C_l$
for $\nu' \in \mathcal{N}(c)$
Compute the MtL translation (30)
5. *Downward Pass.*
for $l = l_{min}, \dots, L - 1$
for $c \in C_l$
for $c' \in \mathcal{K}(c)$
Compute the LtL translation (35)

6. Evaluation Phase.

for $c \in C_L$

 Compute the LtP translation (33)

In this algorithm l_{min} is the coarsest level that contains clusters with non-empty interaction lists.

Since the finest level contain a fixed number of triangles the number of levels grows logarithmically with N as the mesh is refined. With a geometric series argument, one can show that the total number of interaction lists in all levels is $O(N)$. If the translations in all levels are computed with the same order p then the complexity of all translations is $O(Np^3)$. If the variable order method is used where the order is given by (26), then the complexity reduces to $O(N)$. More details can be found in [35].

2.5 Cartesian treecode

The Cartesian treecode can be considered as a fast multipole method without the downward pass. The computational cost of treecode is order of $O(N \log N)$ as opposed to the $O(N)$ FMM. However, the constants in this complexity estimate are smaller, and we found it to be useful for the computation of the free solvation energy (25), where the source and evaluation points are different and zero or limited near field calculations are required. The direct computation of the solvation energy as interactions between N boundary elements and N_c atomic centers has $O(N_c N)$ complexity. This is shown in Fig. 2b, in which a charge located at \mathbf{x}_n will interact with induced charges (ϕ_1 or $\frac{\partial \phi_1}{\partial \nu}$) located at the center of each panel. These interactions consist of near field particle-particle interaction by direction summation and far field particle-cluster interaction controlled by maximum acceptance criterion (MAC) as specified below. For simplicity, we write the involved calculations as

$$E = \sum_{n=1}^{N_c} q_n V_n = \sum_{n=1}^{N_c} q_n \sum_{l=1}^N \int_{\tau_l} \frac{\partial^k}{\partial \nu_{\mathbf{x}}^k} G(\mathbf{x}_n, \mathbf{x}) f(\mathbf{x}) dS_{\mathbf{x}}, \quad (36)$$

where G is Coulomb or screened Coulomb potential kernel, $k \in \{0, 1\}$, q_n 's are partial charges, and f is either ϕ_1 or $\partial \phi_1 / \partial \nu$.

In our implementation, we use the same clustering scheme of Γ_N as in the FMM. Instead of using the interaction lists to calculate the far field interaction, the treecode use the following multipole acceptance criterion (MAC) to determine if the particle and the cluster are well separated or thus a far-field particle-cluster interaction will be considered. This is similar to the separation ratio in the FMM. The MAC is given as

$$\frac{r_c}{R} \leq \theta, \quad (37)$$

where $r_c = \max_{\mathbf{x}_j \in c} |\mathbf{x}_j - \mathbf{x}_c|$ is the cluster radius, $R = |\mathbf{x}_n - \mathbf{x}_c|$ is the particle-cluster distance, and $\theta < 1$ is a user-specified parameter. If the criterion is not satisfied, the program checks the children of the cluster recursively until either the MAC is satisfied or the leaves (the finest level cluster) are reached at which direct summation is applied. Overall, the treecode evaluates the potentials (36) as a combination of particle-cluster interactions and direct summations. Thus, when \mathbf{x}_n and c are well-separated, the potential can be evaluated as

$$\int_c \frac{\partial^k}{\partial \nu_{\mathbf{x}}^k} G(\mathbf{x}_n, \mathbf{x}) f(\mathbf{x}) dS_{\mathbf{x}} \approx \sum_{|\beta|=0}^p D^\beta G(\mathbf{x}_n, \mathbf{x}_c) (-1)^\beta m_c'^\beta(f), \quad (38)$$

where the moment $m_c'^\beta(f)$ is calculated by the same operator-MtM in FMM.

The treecode method therefore can be concluded as

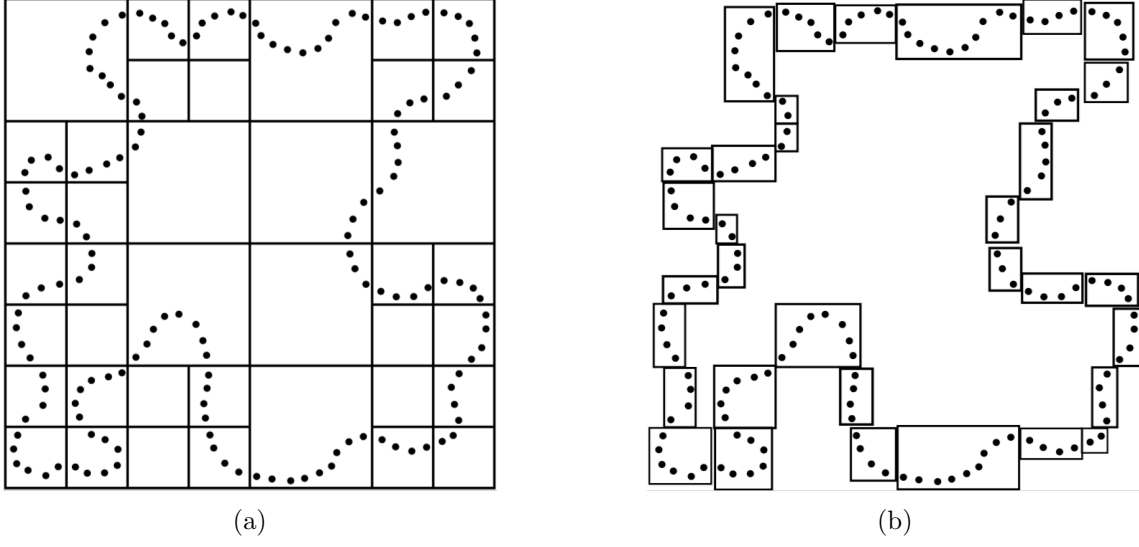


Figure 3: The hierarchical tree structure for the treecode: Left: the form of the tree by recursively dividing a parent cluster into eight/four children clusters using $N_0 = 8$; Right: The adaptive shrink scheme improves the treecode efficiency.

1. *Moment Calculation.*
for $c \in C_L$
Compute the moments $m_{c'}^\beta(f)$ in (32).
2. *Upward Pass.*
for $l = L - 1, \dots, l_{min}$
for $c \in C_l$
for $c' \in \mathcal{K}(c)$
Compute the MtM translation (34)
3. *Interaction Phase*
for $n = 1, \dots, N_c$
 $E_n = 0$
for $c \in C_0$
addCluster(c, \mathbf{x}_n, E_n)

where addCluster(c, \mathbf{x}_n, E_n) as shown below is a routine that recurses from the coarse clusters to the finer clusters until the separation is sufficient to use the Taylor series approximation

if \mathbf{x}_n and \mathbf{x}_c satisfy the MAC for c

$$E_n += \sum_{|\beta|=0}^p D^\beta \Phi(\mathbf{x}_n, \mathbf{x}_c) (-1)^\beta m_c'^\beta(f)$$

else if $\mathcal{K}(c) \neq \emptyset$
for $c' \in \mathcal{K}(c)$
addCluster(c', \mathbf{x}_n, E_n)
else

$$E_n += \int_c \frac{\partial^\kappa}{\partial \nu_{\mathbf{x}}^\kappa} \Phi(\mathbf{x}_n, \mathbf{x}) f(x) dS_{\mathbf{x}}$$

Note that steps 1 and 2 are analogous to the steps the in FMM, hence the addition of the treecode to the FMM code requires little extra work.

2.6 Preconditioning

The results in our previous work [31,49] shows that the PB boundary integral formulation in Eqs. (6a) and (6b) is well-conditioned thus will only require a small number of GMRES iteration if the triangulation quality is satisfied (e.g. nearly quasi-uniform). However, due to the complexity of the molecular surface, the triangulation unavoidably has a few triangles with defects (e.g. narrow triangles and tiny triangles) which deteriorate the condition number of the linear algebraic matrix, resulting in increased GMRES iteration number required to reach the desired convergence accuracy.

Recently, we designed a block-diagonal preconditioning scheme to improve the matrix condition for the treecode-accelerated boundary integral (TABI) Poisson-Boltzmann solver [43]. The essential idea for this preconditioning scheme is to use the short range interactions within the leaves of the tree to form the preconditioning matrix M . This preconditioning matrix M can be permuted into a block diagonal form thus $Mx = y$ can be solved by the efficient and accurate direct methods. In the current study of FAGBI solver, the same conditioning issue rises and it can be resolved by a similar but FMM structure adjusted and controlled preconditioning scheme.

The key idea is to find an approximating matrix M of A such that M is similar to A and the linear system $My = z$ is easy to solve. To this end, our choice for M is the matrix involving only direct sum interactions in cubes/clusters at a designated level (an optimal choice considering both cost and efficiency) as opposed to A , which involves all interactions.

The definition of M will be essentially similar to A in (22) except that the entries of M are zero if τ_i and τ_j are not on the same cube at a designated level of the tree, i.e.

$$M_{mn}(i, j) = \begin{cases} A_{mn}(i, j) & \text{if } \tau_i, \tau_j \text{ are on the same cube at a designated level of the tree} \\ 0 & \text{otherwise.} \end{cases} \quad (39)$$

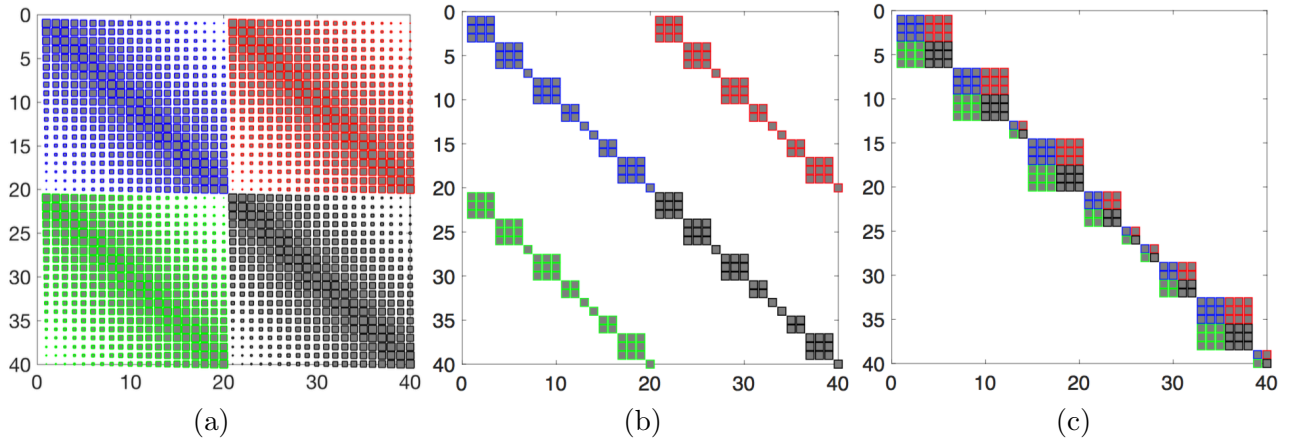


Figure 4: A schematic illustration of the boundary element dense matrix A and its preconditioning matrix M : (a) matrix A for the case of $N = 20$ elements (the size of the matrix entry shows the strength of the interaction; the four different color-coded region relates to K_{1-4} in Eqs. (6a)-(6b)); (b) the “block diagonal block” preconditioning matrix M (assuming the cube at the designated level contains at most 3 panels); (c) the “block diagonal” preconditioning matrix M , which is a permuted matrix from M in (b) after switching the order of the unknowns.

Here we use Fig. 4 to illustrate how we design our preconditioning scheme and its advantage. Figure 4(a) is the illustration of the dense boundary element matrix A for the discretized system (22) with 20 boundary elements. The four different colors represent the four kernels K_{1-4} related entries of the linear algebraic matrix A in Eq. (23). Note the unknowns are ordered by the potentials ϕ_1 on all elements, followed by the normal derivative of the potential $\frac{\partial\phi_1}{\partial\nu}$. The size of the matrix entry in Fig. 4 indicates the magnitude of the interaction between a target element and a source element, which decays from the main diagonal to its two wings. By only including the interactions between elements on the same cube at a designated level, we obtain our designed preconditioning matrix M as illustrated in Fig. 4(b). This preconditioning matrix M has four blocks, and each block is a diagonal block matrix. Following the procedure detailed in [43], by rearranging the order of the unknowns, a block diagonal matrix M is achieved as illustrated in Fig. 4(c). Since $M = \text{diag}\{M_1, M_2, \dots, M_{N_i}\}$ as shown in Fig. 4(c) is a block diagonal matrix such that $My = z$ can be solved using direct method e.g. LU factorization by solving each individual $M_i y_i = z_i$. Here each M_i is a square nonsingular matrix, which represents the interaction between particles/elements on the i th cube of the tree at a designated level. As shown in [43], the total cost of solving $My = z$ is essentially $O(N)$ thus is very efficient. Results for the preconditioning performance will be shown in the next section.

3 Results

Our numerical results are mostly produced on a desktop with an i5 7500 CPU and 16G Memory, using GNU Fortran 7.2.0 compiler with compiling option “-O2”. A few results for the long elapsed direct summation are obtained from the SMU high performance computing cluster, ManeFrame II (M2), with Intel Xeon Phi 7230 Processors, using openmpi/3.1.3 compiler with compiling option “-O2”. Note these direct sum results are needed for the evaluation of accuracy only and low resolutions results are checked on different machines to ensure the consistency of the accuracy. All protein structures are obtained from Protein Data Bank (<https://www.rcsb.org/>) and partial charges are assigned by CHARMM22 force field [50] using PDB2PQR software [51].

The physical quantity we computed in this manuscript is the electrostatic free energy of solvation with the unit kcal/mol. The electrostatic potential ϕ or ϕ_1 governed in Eq. (1) or Eqs. (6a-6b) uses the unit of $e_c/(4\pi\text{\AA})$, where e_c is the elementary charge. By doing this, we can directly use the partial charge obtained from PDB2PQR [51] for solving the PB equation. After obtaining the potential, we can convert the unit $e_c/(4\pi\text{\AA})$ to kcal/mol/ e_c by multiplying the constant $4\pi 332.0716$ at room temperature $T=300\text{K}$. From potential to energy, only a multiplication of e_c is needed.

We solved the PB equation first on the Kirkwood sphere [52], where the analytic solution is available to validate the accuracy and efficiency of FAGBI solver, then on a typical protein 1a63 to demonstrate the overall performance, and finally on a series of proteins to emphasize the preconditioning scheme and the broad usage of the FAGBI solver.

3.1 The Kirkwood sphere

Our first test case is the Kirkwood sphere of radius 50\AA with an atomic charge $q = 50e_c$ at the center of the sphere. The dielectric constant is $\epsilon_1 = 1$ inside the sphere and $\epsilon_2 = 40$ outside the sphere. We provide three parts of this test case on the Kirkwood sphere, which show first the discretization error, then the impact of the quadrature orders toward the convergence of accuracy, and finally the comparison between using the Cartesian FMM and using direct sum in terms of error, CPU time, and memory usage.

3.1.1 Overall discretization error

We first solve the boundary integral PB equation on the Kirkwood sphere using the direct summation for matrix-vector product instead of using the FMM acceleration. The linear algebraic system is solved using GMRES iterative solver with L_2 relative tolerance $\tau = 10^{-6}$. The Galerkin method is applied to form the matrix combined with a single point Gauss quadrature. Cubature methods [47] are applied for treating the singularities arising from Galerkin discretization of boundary integral equations.

Table 1: Discretization error from solving the PB equation on a Kirkwood sphere with a centered charge. Results include electrostatic solvation free energy E_{sol}^{ds} with error e_{sol}^{ds} and convergence rate r_{sol}^{ds} , and discretization error in surface potential e_{ϕ}^{ds} , normal derivative $e_{\partial_n\phi}^{ds}$ with their convergence rates r_{ϕ}^{ds} and $r_{\partial_n\phi}^{ds}$.

N^1	h	E_{sol}^{ds} (kcal/mol)	e_{sol}^{ds} (%)	r_{sol}^{ds}	e_{ϕ}^{ds} (%)	r_{ϕ}^{ds}	$e_{\partial_n\phi}^{ds}$ (%)	$r_{\partial_n\phi}^{ds}$	Iters ²
320	9.90	-8413.28	1.692	3.6	17.925	4.1	0.652	1.9	3
1280	4.95	-8328.18	0.663	2.6	4.419	4.1	0.212	3.1	3
5120	2.48	-8293.42	0.243	2.7	1.112	4.0	0.092	2.3	3
20,480	1.24	-8280.70	0.089	2.7	0.285	3.9	0.046	2.0	3
81,920	0.62	-8276.33	0.036	2.5	0.077	3.7	0.023	2.0	3
327,680	0.31	-8274.64	0.016	2.3	0.022	3.5	0.011	2.0	3
1,310,720	0.15	-8273.91	0.007	2.2	0.007	3.2	0.006	2.0	4
∞^3		-8273.31							

¹ N is number of triangles in triangulation; h is the average of largest edge length of all triangles; $h \approx O(N^{-2})$

² Number of GMRES iterations.

³ This row displays the exact electrostatic solvation energy E_{sol}^{ex} , which is known analytically.

Table 1 shows the total discretization errors, which is related to triangulation, quadrature, and basis function. In this table, Column 1 is the number of triangles N for the sphere with the refinement of the mesh and Column 2 is the average of largest edge length of all triangles h . Note we have $h \approx O(N^{-2})$, which can be seen from the comparison of values in the two columns. Since using N is more convenient to specify mesh refinement in our numerical simulation, we use it to quantify the mesh refinement for the rest of the paper.

Columns 3-4 show that the electrostatic solvation energy E_{sol}^{ds} and its error e_{sol}^{ds} compared with the true value in the last row of the table. The convergence rate r_{sol}^{ds} defined as the ratio of the error is shown in column 5 with an $O(N^{-1/2})$ pattern. The relative L_{∞} errors of surface potential ϕ , e_{ϕ}^{ds} and normal derivative $\partial_n\phi$, $e_{\partial_n\phi}^{ds}$, are shown in columns 6 and 8. The surface potential converges with a pattern of $O(N^{-1})$ as shown in column 7, which is faster than its normal derivative with a pattern of $O(N^{-1/2})$ as shown in column 9. We believe that this is due to the continuity of surface potential and the discontinuity of the normal derivatives across the interface. We also can observe that the GMRES iterations shown in column 10 in all the tests are less than or equal to four, which verifies that the boundary integral formulation is well-posed.

Note a back-to-back comparison between Table 1 in this manuscript and Table 2 in our previous work [31] shows improvements in convergence of E_{sol}^{ds} , ϕ , and $\partial_n\phi$ for the present work. This is due to the Galerkin scheme with Duffy's trick and the Cubature method in treating the singularity as opposed to the collocation scheme with simply the removal of singular integral whenever it occurs on an element [31].

3.1.2 Quadrature error

In part 1, we noticed that the converge rate for E_{sol}^{ds} is about $O(N^{-1/2})$ as the rate of $\partial_n \phi$, but is less than the $O(N^{-1})$ rate of ϕ . To investigate the possible reason, we study the influence of the quadrature rule the next.

We increase the order of the tensor product Gauss-Legendre rule to 2, 3 and 4 and test their effects on the discretization error of E_{sol}^{ds} as shown in Table 2. Comparing with results in Table 1, using higher order quadratures improves both the convergence rate of E_{sol}^{ds} and the required GMRES iterations. When the quadrature order is 4, the electrostatic solvation energy E_{sol}^{ds} converges to the exact energy at the rate $O(N^{-1})$ approximately.

Increasing the quadrature order further will not significantly improve the convergence rate of E_{sol}^{ds} , because then the discretization error will be greater than the quadrature error. Since higher quadrature requires more computational cost, in practice, due to the large size of the protein solvation problem, we will use quadrature order 1 as it shows the optimal combination of accuracy and efficiency.

Table 2: Discretization error of solvation free energy E_{sol}^{ds} for solving the same problem in case 1 using Gaussian quadrature orders of 2-4

N	Quad. Order 2			Quad. Order 3			Quad. Order 4		
	E_{sol}^{ds}	r_{sol}^{ds}	Iters	E_{sol}^{ds}	r_{sol}^{ds}	Iters	E_{sol}^{ds}	r_{sol}^{ds}	Iters
320	-8378.82	3.7	2	-8369.13	3.9	2	-8369.21	3.9	2
1280	-8305.24	3.3	3	-8298.57	3.8	2	-8297.67	4.0	2
5120	-8284.01	3.0	3	-8280.12	3.7	3	-8279.40	3.9	3
20,480	-8277.27	2.7	3	-8275.21	3.6	3	-8374.81	4.0	3
81,920	-8274.94	2.4	3	-8273.89	3.3	3	-8373.68	4.1	3
327,680	-8274.03	2.3	3	-8273.51	3.0	3	-8373.40	4.0	3
1,310,720	-8273.64	2.2	3	-8273.38	2.7	3	-8273.33	4.7	3
∞	-8273.31			-8273.31			-8273.31		

3.1.3 FMM

This part of the test studies the role of Cartesian FMM relating to the accuracy and efficiency of the algorithm. We applied the FMM to replace the direct-sum for accelerating the matrix-product calculation in GMRES. Here we use the first order quadrature rule for simplicity. We set $\eta = 0.8$, which is defined in (28) and adjust the number of levels L in the FMM algorithm for different N . Figure 5 shows (a) the error in electrostatic solvation energy, (b) the CPU time, and (c) the memory usage versus the number of triangles N . Here the error is computed as compared with the exact value $E_{sol}^{ex} = -8273.31$. We provide results using fixed Taylor expansion order $p = 1, 3, 5, 7$ and adaptive order start from $p = 1$, and $p = 3$. Here the adaptive order represents the idea that expansion order should be adjusted to the level (e.g. higher expansion order at higher level) in order to match the discretization error [48]. In this figure, the solid blue line with square marks is results of direct summation with one point quadrature, which shows in (a) an $O(N^{-1/2})$ order of convergence in accuracy as observed in Table 1, an $O(N^2)$ CPU time in (b), and an $O(N)$ memory usage in (c).

As seen in Fig. 5(a), the use of FMM introduces truncation error in addition to the discretization error. Truncation errors are more significant than the discretization error when the order p is small and are less significant when p is large.

Furthermore, we observed that when expansion orders $p = 5, 7$ of the FMM are used, the errors are even smaller than those obtained with the direct sum. This is due to the fact that the error

of the truncation error of Taylor approximation is smaller than the quadrature error of the far field coefficients in the direct sum.

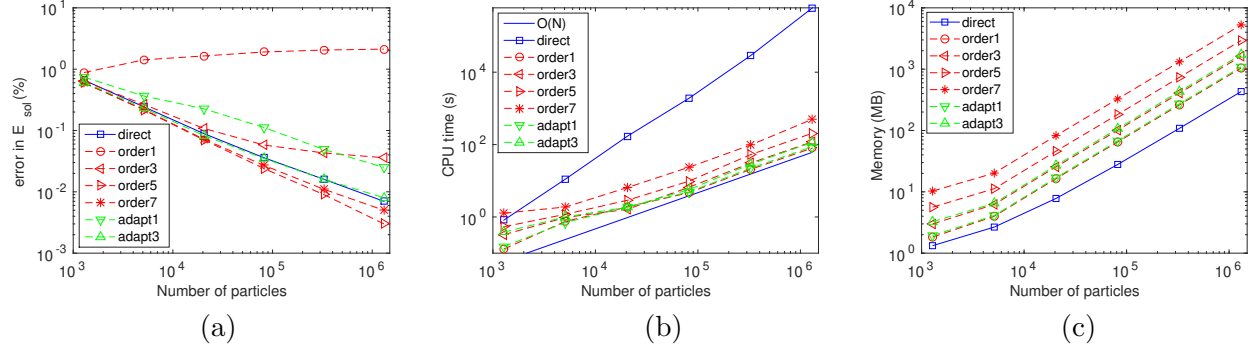


Figure 5: (Compute electrostatic solvation energy on a Kirkwood sphere as number of triangles/particles N in creases: (a) Error, (b) CPU time, and (c) Memory usage; discretization error e_{sol}^{ds} (solid line), Cartesian FMM approximation error e_{sol}^{cf} (dashed line); Taylor expansion order $p = 1, 3, 5, 7$ and adaptive Taylor order $p = 1, 3$

As seen in Fig. 5(b), the use of FMM significantly reduce the CPU time, which shows a $O(N)$ pattern as opposed to the $O(N^2)$ pattern of the direct sum. Figures. 5(a-b) combined also justify the use of adaptive order. Adaptive order 1 and 3 use about the same amount of CPU time as regular order 1 and 3 but achieved significant improvements in accuracy. Meanwhile, Figure 5(c) shows that FMM use additional memory in trading of efficiency. However, the $O(N)$ pattern of memory usage are well preserved at different orders with only an adjustment in a factor.

In summary, from Tables 1 and 2, we observed that the Galerkin discretization with piecewise constant basis functions can achieve $O(N^{-1/2})$ convergence rate with low quadrature order (e.g. 1 or 2) and can achieve $O(N^{-1})$ convergence rate with high quadrature order (e.g. 4). Applying FMM algorithm for acceleration significantly reduced the $O(N^2)$ CPU time to $O(N)$ while maintains desired accuracy and $O(N)$ memory usage. For later tests, we apply the adaptive FMM with starting order 1 and $\eta = 0.8$ as an optimal choice at the consideration of both efficiency and accuracy.

3.2 The protein 1a63

In this section, we use the FAGBI solver to compute the solvation energy for protein 1A63, which has 2065 atoms. In computation involving proteins, the molecular surface is triangulated by MSMS [44], with atom locations from the Protein Data Bank [53] and partial charges from the CHARMM22 force field [50]. MSMS has a user-specified density parameter d controlling the number of vertices per \AA^2 in the triangulation. MSMS constructs an irregular triangulation which becomes smoother as d increases. The tree structure level is adjusted according to different number of particles. The GMRES tolerance is $\tau = 10^{-4}$. These are representative parameter values chosen to ensure that the FMM approximation error and GMRES iteration error are smaller than the direct sum discretization error, and to keep efficient performance in CPU time and memory based on tests on spheres previously.

In Table 3, the first two columns give the MSMS density (d) and number of faces N in the triangulation. The next two columns give the electrostatic solvation energy E_{sol} computed by direct sum (ds) and Cartesian FMM (cf). We use a parallel version of direct sum to compute an estimate of the exact energy with high order quadrature methods. We computed the discretization errors e_{sol}^{ds} and e_{sol}^{cf} on the fifth and sixth columns, which shows convergence rate faster than $O(N^{-1})$ as observed

Table 3: (protein 1A63). FAGBI results; PB equations; showing electrostatic solvation energy E_{sol} , error, CPU time, memory usage; columns show MSMS density (d in \AA^{-2}), number of triangles N , E_{sol} values computed by direct sum (ds) and Cartesian FMM (cf), discretization error e_{sol}^{ds} , Cartesian FMM approximation error e_{sol}^{cf} and their convergence rate r_{sol}^{ds} and r_{sol}^{cf} ; adaptive Taylor expansion order $p = 1$, separate rate $\eta = 0.8$.

d	N^a	E_{sol} (kcal/mol)		Error (%)		Rate		CPU (s)		Mem. (MB)	
		ds	cf	e_{sol}^{ds}	e_{sol}^{cf}	r_{sol}^{ds}	r_{sol}^{cf}	ds	cf	ds	cf
1	20,227	-2755.05	-2756.82	16.12	16.20			632	6	18	30
2	30,321	-2498.20	-2499.20	5.30	5.34	5.5	5.4	1135	8	23	40
5	69,969	-2412.40	-2413.02	1.68	1.71	2.7	2.7	5912	17	66	111
10	132,133	-2383.09	-2382.50	0.45	0.42	4.1	4.4	36,530	37	92	165
20	264,927	-2375.21	-2376.52	0.11	0.17	3.9	2.6	149,651	69	249	423
40	536,781	-2371.52	-2372.77	0.04	0.01	2.9	7.5	618,879	141	359	654
	∞^b	-2372.48	-2372.48								

^a Number of elements in triangulation.

^b This row shows the estimates of exact energy E_{sol}^{ex} obtained by the parallel computing on high order quadrature method.

for the geodesic grid triangulation of the Kirkwood sphere in Case 1. The faster convergence seen here is due to non-uniform adaptive treatment of MSMS triangulation [31].

A back-to-back comparison of results from direct sum (ds) and Cartesian FMM results cf in Error, Rate, CPU time, and Memory in table 3 provides the following conclusions. (1) the adoption of FMM only slightly modify the error and its convergence rate in accuracy, not even necessarily in a negative way; (2) Cartesian FMM dramatically reduces the $O(N^2)$ direct sum CPU time to $O(N)$. For example, the simulation with $d = 10\text{\AA}^{-2}$ and $N = 132,133$ took $36,530\text{s} \approx 10\text{h}$ by direct sum and $37\text{s} \approx 1/2\text{min}$ by FMM; (3) Moreover, the memory usage shows that both the direct sum and FMM memory usage is $O(N)$. For the FMM, more memory is used for the moment and local coefficient storage but this only adds a pre-factor rather than increases the growth rate.

3.3 27 proteins

We finally provide testing results on a set of 27 proteins for the purpose of demonstrating the general application of FAGBI solver to broader macromolecules and the efficiency of the preconditioning scheme. Table 4 shows the convergence tests using diagonal preconditioning (d) and block diagonal preconditioning (bd) for a set of 27 proteins. After applying the block diagonal preconditioning scheme, the cases with slow convergence using diagonal preconditioning has been well resolved. In this table, the first column is the protein index, followed by the PDB ID in the second column, and the number of elements in the third column generated by MSMS with density $d = 10$. Columns 4 and 5 are the solvation energy of the proteins applying both preconditioning schemes, and column 6 is the relative difference between both methods, which shows no significant difference. A significant reduction of number of iterations using block diagonal preconditioning (bd) is shown in column 8 compared with results in column 7 using diagonal preconditioning (d). One can see that the worse the diagonal preconditioning result is, the larger improvements block diagonal preconditioning can achieve. For example, proteins 2pde, 1sh1, 1a7m, 2go0, 1uv0 and 4mth first use 75, 100, 55, 44, 73, and 36 iterations for diagonal preconditioning as highlighted in column 7, but only use 23, 21, 21,

Table 4: Convergence comparison using diagonal preconditioning (d) and block diagonal preconditioning (bd) on a set of 27 proteins; MSMS density $d = 10$.

Ind.	PDB	# of ele.	E_{sol} (kcal/mol)			# of it.		CPU time (s)		
			d	bd	diff. (%)	d	bd	d	bd	ratio
1	1ajj	40496	-1141.17	-1141.15	0.00	22	14	12.5	9.7	1.28
2	2erl	43214	-953.43	-953.42	0.00	15	10	9.2	7.8	1.18
3	1cbn	44367	-305.94	-305.94	0.00	12	11	7.4	8.3	0.88
4	1vii	47070	-906.11	-906.11	0.00	16	14	10.6	11.5	0.92
5	1fca	47461	-1206.46	-1206.48	0.00	16	11	10.2	8.8	1.16
6	1bbl	49071	-991.21	-991.22	0.00	19	13	13.3	11.2	1.18
7	2pde	50518	-829.49	-829.46	0.00	75	23	50.7	19.5	2.60
8	1shl	51186	-756.64	-756.63	0.00	100	21	70.7	18.2	3.89
9	1vjw	52536	-1242.55	-1242.56	0.00	11	10	8.2	9.3	0.87
10	1uxc	53602	-1145.38	-1145.38	0.00	20	13	14.7	11.9	1.23
11	1ptq	54256	-877.83	-877.84	0.00	16	13	11.9	12.2	0.97
12	1bor	54628	-857.28	-857.27	0.00	14	13	10.9	12.5	0.87
13	1fxd	54692	-3318.18	-3318.14	0.00	10	10	7.8	9.9	0.79
14	1r69	57646	-1094.86	-1094.86	0.00	13	12	10.6	12.6	0.84
15	1mbg	58473	-1357.32	-1357.33	0.00	18	13	14.8	13.6	1.09
16	1bpi	60600	-1309.61	-1310.02	0.03	18	12	16.2	14.5	1.11
17	1hpt	61164	-816.47	-817.34	0.11	15	13	12.8	14.0	0.92
18	451c	79202	-1031.74	-1031.91	0.02	27	20	30.3	28.8	1.05
19	1svr	88198	-1718.97	-1718.97	0.00	15	12	21.4	21.3	1.01
20	1frd	81792	-2868.29	-2867.32	0.00	14	12	18.1	17.2	1.05
21	1a2s	84527	-1925.23	-1925.24	0.00	20	17	26.4	24.8	1.06
22	1neq	89457	-1740.50	-1740.49	0.00	19	15	26.7	22.8	1.17
23	1a63	132133	-2382.50	-2382.50	0.00	21	16	41.3	36.8	1.12
24	1a7m	147121	-2171.13	-2172.12	0.00	55	21	111.2	51.4	2.16
25	2go0	111615	-1968.61	-1968.65	0.00	44	24	67.6	43.0	1.57
26	1uv0	128497	-2296.43	-2296.43	0.00	73	25	130.7	52.6	2.48
27	4mth	123737	-2479.62	-2479.61	0.00	36	18	64.3	37.0	1.74

24, 25, and 18 iterations for block diagonal preconditioning. The CPU time comparison in columns 9 and 10, as well as their ratio in column 11, further confirms the results in columns 7 and 8 as CPU time is related to the number of iterations. The ratio of CPU reduction for some proteins are more than 2 times as highlighted in the last column. We plot the results of columns 7,8,9 and 10 in Fig. 6 which shows the improvements on both number of iterations and CPU time when block diagonal preconditioning is used to replace the diagonal preconditioning. It shows that the block diagonal preconditioning does not impair the originally well-conditioned cases but significantly improve the slow convergence cases, which suggests that we can uniformly use block diagonal preconditioning in replace of the original diagonal preconditioning. Figures 6(a) and 6(b) shows a similar pattern as CPU time and the number of iterations are highly correlated.

4 Conclusion

In this paper, we report recent work in developing an FMM accelerated Galerkin boundary integral (FAGBI) method for solving the Poisson-Boltzmann equation. The solver has combined advantages in accuracy, efficiency, and memory as it applies a well-posed boundary integral formulation to circum-

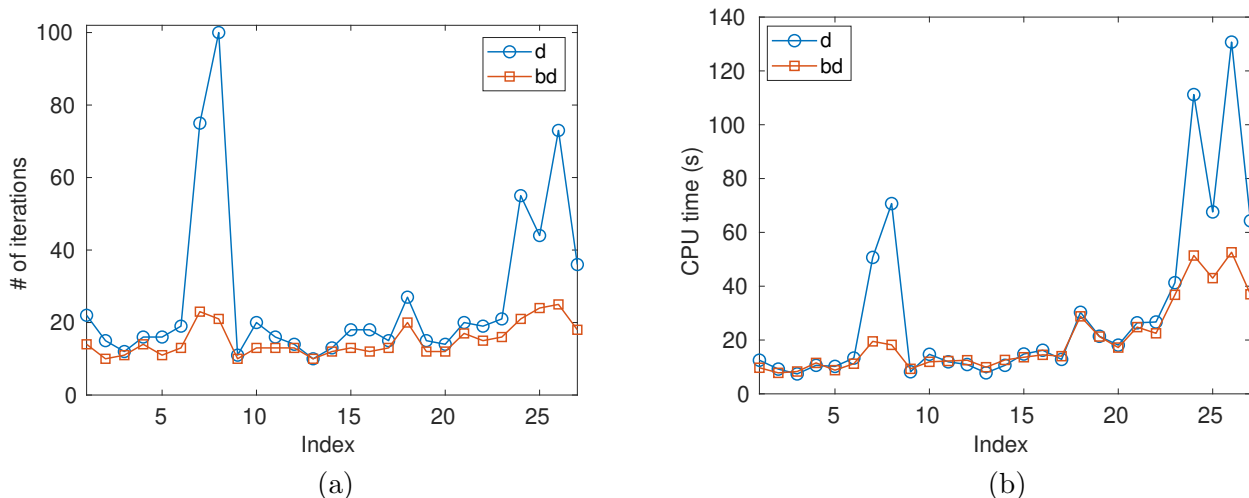


Figure 6: convergence comparison using diagonal preconditioning and block diagonal preconditioning. (a) number of iterations; (b) CPU time (s).

vent many numerical difficulties and uses an $O(N)$ Cartesian FMM to accelerate the GMRES iterative solver. Special treatments such as adaptive FMM order, block diagonal preconditioning, Galerkin discretization, and Duffy’s transformation are combined to improve the performance, which is validated on benchmark Kirkwood’s sphere and a series of testing proteins. With its attractive $O(N^{-1})$ convergence rate in accuracy, $O(N)$ CPU run time, and $O(N)$ memory usage, the FAGBI solver and its broad usage can contribute significantly to the greater computational biophysics/biochemistry community as a powerful tool for the study of electrostatics of solvated biomolecules.

Acknowledgments

The work of W.G. and J.C. was supported by NSF grant DMS-1418957, DMS-1819193, SMU new faculty startup fund and SMU center for scientific computing. The work of J.T. is in part funded by NSF grant DMS-1720431.

References

- [1] N. A. Baker, “Improving implicit solvent simulations: a Poisson-centric view,” *Curr. Opin. Struct. Biol.*, vol. 15, no. 2, pp. 137–43, 2005.
- [2] V. Cherezov, D. M. Rosenbaum, M. A. Hanson, S. G. F. Rasmussen, F. S. Thian, T. S. Kobilka, H.-J. Choi, P. Kuhn, W. I. Weis, B. K. Kobilka, and R. C. Stevens, “High-resolution crystal structure of an engineered human beta2-adrenergic g protein-coupled receptor,” *Science*, vol. 318, no. 5854, pp. 1258–1265, 2007.
- [3] N. Huang, Y. Chelliah, Y. Shan, C. A. Taylor, S.-H. Yoo, C. Partch, C. B. Green, H. Zhang, and J. S. Takahashi, “Crystal structure of the heterodimeric CLOCK:BMAL1 transcriptional activator complex,” *Science*, vol. 337, no. 6091, pp. 189–194, 2012.

- [4] D. A. Beard and T. Schlick, “Modeling salt-mediated electrostatics of macromolecules: the discrete surface charge optimization algorithm and its application to the nucleosome,” *Biopolymers*, vol. 58, pp. 106–115, 2001.
- [5] E. Alexov, E. L. Mehler, N. Baker, A. M. Baptista, Y. Huang, F. Milletti, J. E. Nielsen, D. Farrell, T. Carstensen, M. H. M. Olsson, J. K. Shen, J. Warwicker, S. Williams, and J. M. Word, “Progress in the prediction of pka values in proteins,” *Proteins*, vol. 79, pp. 3260–3275, Dec 2011.
- [6] J. Hu, S. Zhao, and W. Geng, “Accurate pka computation using matched interface and boundary (MIB) method based Poisson-Boltzmann solver,” *Communication in Computational Physics*, vol. 2, pp. 520–539, 2018.
- [7] J. Chen, J. Hu, Y. Xu, R. Krasny, and W. Geng, “Computing protein pKas using the TABI Poisson-Boltzmann solver,” *J. Comput. Biophys. Chem.*, vol. 20, no. 2, pp. 175–187, 2021.
- [8] Y. C. Zhou, B. Lu, and A. A. Gorfe, “Continuum electromechanical modeling of protein-membrane interactions,” *Phys. Rev. E*, vol. 82, p. 041923, Oct 2010.
- [9] D. D. Nguyen, B. Wang, and G.-W. Wei, “Accurate, robust, and reliable calculations of Poisson-Boltzmann binding energies,” *Journal of Computational Chemistry*, vol. 38, no. 13, pp. 941–948, 2017.
- [10] J. A. Wagoner and N. A. Baker, “Assessing implicit models for nonpolar mean solvation forces: The importance of dispersion and volume terms,” *Proceedings of the National Academy of Sciences*, vol. 103, no. 22, pp. 8331–8336, 2006.
- [11] N. Unwin, “Refined structure of the nicotinic acetylcholine receptor at 4Å resolution,” *Journal of Molecular Biology*, vol. 346, no. 4, pp. 967 – 989, 2005.
- [12] N. A. Baker, “Poisson-Boltzmann methods for biomolecular electrostatics,” *Methods Enzymol.*, vol. 383, pp. 94–118, 2004.
- [13] W. Im, D. Beglov, and B. Roux, “Continuum solvation model: electrostatic forces from numerical solutions to the Poisson-Boltzmann equation,” *Computer Physics Communications*, vol. 111, no. 1-3, pp. 59–75, 1998.
- [14] B. Honig and A. Nicholls, “Classical electrostatics in biology and chemistry,” *Science*, vol. 268, no. 5214, pp. 1144–9, 1995.
- [15] N. A. Baker, D. Sept, S. Joseph, M. J. Holst, and J. A. McCammon, “Electrostatics of nanosystems: Application to microtubules and the ribosome,” *Proc. Natl. Acad. Sci. U. S. A.*, vol. 98, no. 18, pp. 10037–10041, 2001.
- [16] R. Luo, L. David, and M. K. Gilson, “Accelerated Poisson-Boltzmann calculations for static and dynamic systems,” *Journal of Computational Chemistry*, vol. 23, no. 13, pp. 1244–53, 2002.
- [17] W. Deng, X. Zhufu, J. Xu, and S. Zhao, “A new discontinuous galerkin method for the nonlinear Poisson-Boltzmann equation,” *Applied Mathematics Letters*, vol. 257, pp. 1000–1021, 2015.
- [18] J. Ying and D. Xie, “A new finite element and finite difference hybrid method for computing electrostatics of ionic solvated biomolecule,” *Journal of Computational Physics*, vol. 298, pp. 636 – 651, 2015.

- [19] Z. Qiao, Z. Li, and T. Tang, “Finite difference scheme for solving the nonlinear poisson-boltzmann equation modeling charged spheres,” *Journal of Computational Mathematics*, vol. 24, 04 2006.
- [20] S. Yu, W. Geng, and G. W. Wei, “Treatment of geometric singularities in implicit solvent models,” *Journal of Chemical Physics*, vol. 126, p. 244108, 2007.
- [21] W. Geng, S. Yu, and G. W. Wei, “Treatment of charge singularities in implicit solvent models,” *J. Chem. Phys.*, vol. 127, p. 114106, 2007.
- [22] Q. Cai, J. Wang, H.-K. Zhao, and R. Luo, “On removal of charge singularity in Poisson-Boltzmann equation,” *The Journal of Chemical Physics*, vol. 130, no. 14, 2009.
- [23] W. Geng and S. Zhao, “A two-component matched interface and boundary (mib) regularization for charge singularity in implicit solvation,” *J. Comput. Phys.*, vol. 351, pp. 25–39, 2017.
- [24] A. Lee, W. Geng, and S. Zhao, “Regularization methods for the Poisson-Boltzmann equation: comparison and accuracy recovery,” *J. Comput. Phys.*, vol. 426, p. 109958, 2020.
- [25] A. Juffer, B. E., B. van Keulen, A. van der Ploeg, and H. Berendsen, “The electric potential of a macromolecule in a solvent: a fundamental approach,” *J. Comput. Phys.*, vol. 97, pp. 144–171, 1991.
- [26] A. H. Boschitsch, M. O. Fenley, and H.-X. Zhou, “Fast boundary element method for the linear Poisson-Boltzmann equation,” *The Journal of Physical Chemistry B*, vol. 106, no. 10, pp. 2741–2754, 2002.
- [27] B. Lu, X. Cheng, and J. A. McCammon, “A new-version-fast-multipole-method-accelerated electrostatic calculations in biomolecular systems,” *Journal of Computational Physics*, vol. 226, no. 2, pp. 1348 – 1366, 2007.
- [28] L. Greengard, D. Gueyffier, P.-G. Martinsson, and V. Rokhlin, “Fast direct solvers for integral equations in complex three-dimensional domains,” *Acta Numerica*, vol. 18, pp. 243–275, 005 2009.
- [29] C. Bajaj, S.-C. Chen, and A. Rand, “An efficient higher-order fast multipole boundary element solution for Poisson-Boltzmann-based molecular electrostatics,” *SIAM Journal on Scientific Computing*, vol. 33, no. 2, pp. 826–848, 2011.
- [30] B. Zhang, B. Lu, X. Cheng, J. Huang, N. P. Pitsianis, X. Sun, and J. A. McCammon, “Mathematical and numerical aspects of the adaptive fast multipole Poisson-Boltzmann solver,” *Communications in Computational Physics*, vol. 13, pp. 107–128, 001 2013.
- [31] W. Geng and R. Krasny, “A treecode-accelerated boundary integral Poisson-Boltzmann solver for electrostatics of solvated biomolecules,” *Journal of Computational Physics*, vol. 247, pp. 62 – 78, 2013.
- [32] Y. Zhong, K. Ren, and R. Tsai, “An implicit boundary integral method for computing electric potential of macromolecules in solvent,” *Journal of Computational Physics*, vol. 359, pp. 199 – 215, 2018.
- [33] C. Quan, B. Stamm, and Y. Maday, “A domain decomposition method for the Poisson-Boltzmann solvation models,” *SIAM Journal on Scientific Computing*, vol. 41, no. 2, pp. B320–B350, 2019.

- [34] L. F. Greengard and J. Huang, “A new version of the fast multipole method for screened coulomb interactions in three dimensions,” *J. Comput. Phys.*, vol. 180, no. 2, pp. 642 – 658, 2002.
- [35] J. Tausch, “The variable order fast multipole method for boundary integral equations of the second kind,” *Computing*, vol. 72, no. 3, pp. 267–291, 2004.
- [36] J. Barnes and P. Hut, “A hierarchical $O(N \log N)$ force-calculation algorithm,” *Nature*, vol. 324, pp. 446–449, 12 1986.
- [37] P. Li, H. Johnston, and R. Krasny, “A Cartesian treecode for screened Coulomb interactions,” *J. Comput. Phys.*, vol. 228, no. 10, pp. 3858–3868, 2009.
- [38] L. Wang, R. Krasny, and S. Tlupova, “A kernel-independent treecode based on barycentric lagrange interpolation,” *Commun. Comput. Phys.*, vol. 28, no. 4, pp. 1415–1436, 2020.
- [39] J. Chen, W. Geng, and D. Reynolds, “Cyclically paralleled treecode for fast computing electrostatic interactions on molecular surfaces,” *Comput. Phys. Commun.*, vol. 260, p. 107742, 2021.
- [40] N. A. Baker, D. Sept, M. J. Holst, and J. A. Mccammon, “The adaptive multilevel finite element solution of the Poisson-Boltzmann equation on massively parallel computers,” *IBM Journal of Research and Development*, vol. 45, no. 3-4, pp. 427–438, 2001.
- [41] E. Jurrus, D. Engel, K. Star, K. Monson, J. Brandi, L. E. Felberg, D. H. Brookes, L. Wilson, J. Chen, K. Liles, M. Chun, P. Li, D. W. Gohara, T. Dolinsky, R. Konecny, D. R. Koes, J. E. Nielsen, T. Head-Gordon, W. Geng, R. Krasny, G.-W. Wei, M. J. Holst, J. A. McCammon, and N. A. Baker, “Improvements to the APBS biomolecular solvation software suite,” *Protein Science*, vol. 27, pp. 112–128, 2018.
- [42] M. G. Duffy, “Quadrature over a pyramid or cube of integrands with a singularity at a vertex,” *SIAM Journal on Numerical Analysis*, vol. 19, no. 6, pp. 1260–1262, 1982.
- [43] J. Chen and W. Geng, “On preconditioning the treecode-accelerated boundary integral (TABI) Poisson-Boltzmann solver,” *J Comput Phys*, vol. 373, pp. 750–762, 2018.
- [44] M. F. Sanner, A. J. Olson, and J. C. Spehner, “Reduced surface: An efficient way to compute molecular surfaces,” *Biopolymers*, vol. 38, pp. 305–320, 1996.
- [45] F. Dong, M. Vijaykumar, and H. X. Zhou, “Comparison of calculation and experiment implicates significant electrostatic contributions to the binding stability of barnase and barstar,” *Biophys. J.*, vol. 85, no. 1, pp. 49–60, 2003.
- [46] S. Rjasanow and O. Steinbach, *The fast solution of boundary integral equations*. Springer, 2006.
- [47] S. A. Sauter, “Cubature techniques for 3-d galerkin bem,” *Boundary Elements: Implementation and Analysis of Advanced Algorithms*, vol. 50, pp. 29–44, 1996.
- [48] J. Tausch, “The fast multipole method for arbitrary Green’s functions,” *Contemporary Mathematics*, vol. 329, pp. 307–314, 2003.
- [49] W. Geng and F. Jacob, “A GPU-accelerated direct-sum boundary integral Poisson-Boltzmann solver,” *Comput. Phys. Commun.*, vol. 184, no. 6, pp. 1490 – 1496, 2013.
- [50] B. R. Brooks, R. E. Bruccoleri, B. D. Olafson, D. States, S. Swaminathan, and M. Karplus, “CHARMM: A program for macromolecular energy, minimization, and dynamics calculations,” *J. Comput. Chem.*, vol. 4, pp. 187–217, 1983.

- [51] T. J. Dolinsky, P. Czodrowski, H. Li, J. E. Nielsen, J. H. Jensen, G. Klebe, and N. A. Baker, “PDB2PQR: expanding and upgrading automated preparation of biomolecular structures for molecular simulations,” *Nucleic Acids Res.*, vol. 35, 2007.
- [52] J. G. Kirkwood, “Theory of solution of molecules containing widely separated charges with special application to zwitterions,” *J. Comput. Phys.*, vol. 7, pp. 351 – 361, 1934.
- [53] <http://www.rcsb.org/pdb/home/home.do>.